INTERNATIONAL JOURNAL OF
NUMERICAL ANALYSIS AND MODELING
Volume 8, Number 4, Pages 584–598

© 2011 Institute for Scientific
Computing and Information

BARYCENTRIC COORDINATE BASED MIXED FINITE ELEMENTS ON QUADRILATERAL/HEXAHEDRAL MESH

RUNHILD A. KLAUSEN, SISSEL S. MUNDAL, AND HELGE K. DAHLE

Abstract. This paper presents barycentric coordinate interpolation reformulated as bilinear and trilinear mixed finite elements on quadrilateral and hexahedral meshes. The new finite element space is a subspace of H(div). Barycentric coordinate interpolations of discrete vector field with node values are also known as the corner velocity interpolation. The benefit of this velocity interpolation is that it contains the constant vector fields (uniform flow). We provide edge based basis functions ensuring the same interpolation, and show how these basis functions perform as separate velocity elements.

Key Words. barycentric coordinate, corner velocity interpolation, mixed finite elements.

1. Introduction

The mixed finite element methods, e.g. [5] and streamline based simulations, [7], are commonly used in engineering applications like reservoir simulation. Consider the Raviart-Thomas or Raviart-Thomas-Nédélec conforming elements in 2 and 3 dimensions respectively denoted the $\mathcal{RT}_r$ and $\mathcal{RTN}_0$, cf. [22, 26, 17]. Because of complex reservoir geology, reliable flow simulations will in general require flexibility in the meshes. In streamline simulations extensions of the $\mathcal{RT}_0$-elements are used to interpolate the velocity field on irregular grids, see [6, 8, 9, 10, 13, 14, 15, 16, 20, 21]. However, the $\mathcal{RT}_r$- and $\mathcal{RTN}_0$-elements do not preserve constant vector fields (uniform flow) in their interpolation space, [16]. As a consequence they exhibit optimal-order convergence for the velocity in $H(\mathrm{div})$, the velocity space, on general meshes, [2, 24].

To circumvent this problem and to improve the accuracy of streamline simulations, Hægland et al. devised the $\mathcal{CVI}$ (corner velocity interpolation) method [8] based on edge fluxes and bilinear or trilinear barycentric vertex interpolation. Barycentric coordinates $\phi_j(\boldsymbol{x})$ on a cell with vertex $\boldsymbol{x}_j$, $j = 1\ldots, n$ is the unique solution of $\sum \boldsymbol{x}_j\phi_j(\boldsymbol{x}) = \boldsymbol{x}$ and $\sum \phi = 1$, cf. [5] among many standard books. Over a triangle these are linear functions, scaled to be one or zero in the vertices. Barycentric coordinates offer linear precision, and used for interpolation of a velocity vector from the vertex values, this would clearly also reproduce a constant velocity field.

In this paper we take an alternative approach and propose a new multi-linear $H(\mathrm{div})$ finite elements on quadrilateral and hexahedral meshes based on the idea of corner velocity interpolation. Hence, rather than constructing a velocity-interpolation that preserve the constant vectors based on given fluxes as a post processing step,

Received by the editors September 7, 2009 and, in revised form, may 22, 2011.
2000 *Mathematics Subject Classification.* 76S05, 74Sxx, 81T80.

we provide edge based shape functions for the $\mathcal{CVI}$. We then employ these functions as the velocity space in a mixed formulation. Some analysis of this velocity space is shown, and we provide a numerical study demonstrating properties of the new elements.

For completeness we review some of the main results on mixed finite elements related to convergence and reproduction of uniform flow on general meshes: Construction of robust $H(\mathrm{div})$-conforming mixed elements on deformed mesh, like quadrilaterals or hexahedra has been addressed by many authors over the last years, among many others see for instance [2, 3, 16, 24, 27] Construction of a finite element subspace of $H(\mathrm{div})$ relies on a multi-linear map to a unit reference cell. The *Piola transformation* relates the reference shape functions to the approximation space on the arbitrary irregular cell in physical space in a manner that preserves the fluxes. For general quadrilaterals, an analysis of vector fields defined via the Piola mapping by Arnold et al. [2], demonstrates a degradation of $H(\mathrm{div}, \Omega)$ convergence compared to rectangular meshes. The $\mathcal{RT}_0$ elements on shape-regular quadrilaterals, do in fact not converge in $H(\mathrm{div}, \Omega)$. For a vector field $\boldsymbol{v}$, the $L^2(\Omega)$ estimate is of optimal-order h, with some additional regularity requirements. In the $L^2(\Omega)$ estimate of the divergence of $\boldsymbol{v}$, on the other hand, accuracy of the interpolation is lost, and hence convergence is lost. This result was not fully resolved before the analysis given in [2].

However, in $L^2(\Omega)$, the $\mathcal{RT}_0$ elements retain optimal-order convergence for both the scalar and the vector fields [24]. Also, what usually is established is convergence in $H(\mathrm{div}, \Omega)$ for smooth grids, or for a sequence of h^2-uniform grids. I.e.; grids asymptotically reaching parallelogram meshes. The discrete fluxes from the $\mathcal{RT}$ element can immediately also be post-processed with an alternative cell interpolation, related to the Arnold-Boffi-Falk elements proposed in [2], to retain full $H(\mathrm{div})$ convergence on general rough meshes, c.f., [12]. Moreover, in [2] they show that for full $H(\mathrm{div})$ convergence of finite element soultions built on the Piola mapping, the lowest-order discrete space on $\mathcal{R}$ has to contain the constants. By exact representation of uniform flow, we ensure reproduction of constants on the physical space instead.

Similar results was obtained for the $\mathcal{RTN}_0$ space on hexahedra meshes in [3]. They prove convergence in $H(\mathrm{div}, \Omega)$ for shape-regular asymptotically parallelepiped meshes. Numerical experiments support this result by indicating no $H(\mathrm{div}, \Omega)$ convergence for meshes of trapezoidal shape. These meshes are conceptually similar to the trapezoidal meshes used in [2], which yield the same numerical results for 2D $\mathcal{RT}_0$ elements. The lack of convergence for the $\mathcal{RTN}_0$ space on general hexahedra meshes is also demonstrated in, e.g., [23]. This deficiency of the $\mathcal{RTN}_0$ velocity space, can be associated to the lack of reproduction of uniform flow. In [16], it is shown that, on a general hexahedron, a constant flow field does not imply linear face fluxes. Hence, the $\mathcal{RTN}_0$ velocity space obtained via the Piola mapping, which implicitly yields a linear flux reconstruction, does not contain the constant functions. The findings in [19] generalize this observation. They prove that for a general hexahedron with bilinear faces, both a local reconstruction of velocity based on the six face fluxes and exact representation of uniform flow (constant velocity field), can not be satisfied in $H(\mathrm{div}, \Omega)$.

The rest of this paper is organized as follows; In the next section we define the preliminaries. Then, in section 3, we present the new $\mathcal{CVI}$ finite element space, and furthermore in section 3.1, we find that the $\mathcal{CVI}$ space can be regarded as a perturbation of the $\mathcal{RT}_0$ elements. Section 3.2 provides the $\mathcal{CVI}$ shape functions for

hexahedra elements. In section 4 we present numerical results for general quadrilateral meshes, and finally the convergence behavior of the $\mathcal{CVI}$ mixed finite element method is summarized, and compared to the $\mathcal{RT}_0$ mixed finite element method.

2. Preliminaries

Let $\Omega \subset \mathbb{R}^d$, with $d = 2, 3$, be a bounded domain, with polygonal boundary $\partial\Omega$. We limit the discussion to the steady-state incompressible single phase flow problem

$$\begin{aligned} -\operatorname{div}(\boldsymbol{K}(\boldsymbol{x})\operatorname{grad} p) &= g, \quad \text{for } \boldsymbol{x} \in \Omega, \\ p(\boldsymbol{x}) &= p_0, \quad \text{for } \boldsymbol{x} \in \partial\Omega. \end{aligned} \tag{1}$$

For applications in reservoir simulation, Equation (1) is to be viewed as a model equation for the pressure, and it is based on an underlying principle of conservation of mass. We denote by p the pressure, and by $\boldsymbol{K}$ the symmetric positive definite diffusion tensor. To account for a general reservoir geology, we allow for the diffusion coefficients to be discontinuous. The geology of this kind of problems also require the use of rough grids, with general hexahedral cells. Finally, any sources or sinks present are represented by $g \in L^2(\Omega)$.

A mixed finite element formulation of (1) is generally based on a variational principle utilizing the space of $L^2(\Omega)$ vector functions. We define the space as follows

$$H(\operatorname{div}, \Omega) = \{\boldsymbol{v} \in (L^2(\Omega))^d \mid \operatorname{div} \boldsymbol{v} \in L^2(\Omega)\},$$

where $L^2(\Omega)$ is the set of square Lebesgue integrable functions on Ω, with norm defined via the inner product, $\|\cdot\|^2_{L^2(\Omega)} = (\cdot,\cdot)_{L^2(\Omega)}$. For brevity, we denote the $L^2(\Omega)$ inner product by $(\cdot,\cdot)$ henceforth. The norm in $H(\operatorname{div}, \Omega)$ is provided by

$$\|\boldsymbol{v}\|^2_{H(\operatorname{div},\Omega)} = \|\boldsymbol{v}\|^2_{L^2(\Omega)} + \|\operatorname{div} \boldsymbol{v}\|^2_{L^2(\Omega)}.$$

Finally, let $< \cdot, \cdot >$ be the $L^2(\partial\Omega)$ inner product.

Let $\boldsymbol{q} = -\boldsymbol{K} \operatorname{grad} p$ denote the unknown fluid velocity. A variational formulation of the problem (1) then reads: *Find a pair* $(\boldsymbol{q}, p) \in H(\operatorname{div}, \Omega) \times L^2(\Omega)$ *such that*

$$\begin{aligned} (\boldsymbol{K}^{-1}\boldsymbol{q}, \boldsymbol{v}) - (p, \operatorname{div} \boldsymbol{v}) &= - < \boldsymbol{v} \cdot \boldsymbol{n}, p_0 >, \quad \forall\, \boldsymbol{v} \in H(\operatorname{div}, \Omega), \\ (\operatorname{div} \boldsymbol{q}, u) &= (g, u), \qquad\qquad \forall\, u \in L^2(\Omega). \end{aligned} \tag{2}$$

2.1. Quadrilateral Meshes. For the sake of simplicity we assume $\Omega \subset \mathbb{R}^2$, until further. Let $\{\mathcal{T}_h\}$ denote a family of partitions of Ω into regular quadrilateral cells, i.e.; all cells are convex, the angles are uniformly bounded away from zero and π, and the ratio between the length of the smallest edge and the diameter of the cell is uniformly bounded from below. Then an element $E \in \mathcal{T}_h$ is of general quadrilateral shape, with h being the maximum element edge. Finally, denote by $\mathcal{E}_h$ the set of all element edges in $\mathcal{T}_h$.

In a mixed setting, the finite element space $V_h \subset H(\operatorname{div}, \Omega)$ is generally defined in terms of shape functions on an element $\hat{E}$ in a reference space $\mathcal{R}$. An arbitrary quadrilateral cell $E \in \mathcal{T}_h$ is thus the image of the reference element $\hat{E}$ via the bilinear map $\boldsymbol{F} = \boldsymbol{F}_E : \hat{E} \to E$, which is smooth and invertible, see Figure 1. Here, $\hat{E} = (0,1) \times (0,1)$ is the unit square.

We denote by $\boldsymbol{x}_{ij}$, $i, j = 0, 1$, the vertices of element E as shown in Figure 1. Let $(\hat{x}, \hat{y}) \in \hat{E}$. The bilinear map reads

$$\boldsymbol{F}_E(\hat{x}, \hat{y}) = \boldsymbol{x}_{00}(1-\hat{x})(1-\hat{y}) + \boldsymbol{x}_{10}\hat{x}(1-\hat{y}) + \boldsymbol{x}_{11}\hat{x}\hat{y} + \boldsymbol{x}_{01}(1-\hat{x})\hat{y}. \tag{3}$$

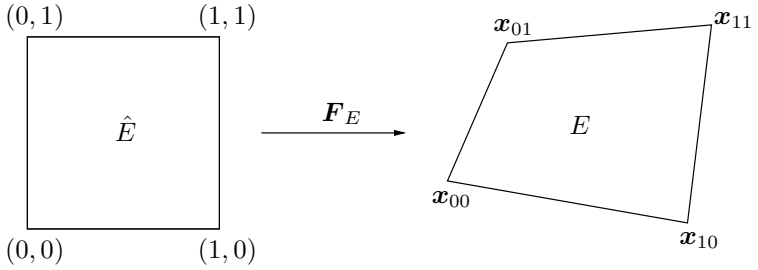

FIGURE 1. A quadrilateral cell E is seen as the image of a reference unit square under the bilinear map $\boldsymbol{F}_E : \hat{E} \to E$.

Any point $\boldsymbol{x} \in E$ can thus be expressed as

$$\boldsymbol{x}(\hat{x}, \hat{y}) = \sum_{ij=1}^{2} \boldsymbol{x}_{ij} \phi_{ij}(\hat{x}, \hat{y}), \tag{4}$$

where the $\phi_{ij} > 0$ are the nodal functions of the bilinear mapping, or bilinear barycentric functions. Given the nodes $\boldsymbol{x}_{kl}$, we have $\phi_{ij}(\boldsymbol{x}_{kl}) = \delta_{(ij)(kl)}$, with $i, j, k, l = 1, 2$, and further

$$\sum_{ij=1}^{2} \phi_{ij}(\hat{x}, \hat{y}) = 1. \tag{5}$$

The latter is needed to exactly represent uniform flow.

The Jacobian matrix of $\boldsymbol{F}_E$ is denoted by $\boldsymbol{D} = D\boldsymbol{F}_E(\hat{\boldsymbol{x}})$ with a strictly positive Jacobian $J = \det \boldsymbol{D} > 0$ for all $\hat{\boldsymbol{x}} \in \hat{E}$.

Also, we will henceforth assume the partitions $\{\mathcal{T}_h\}$ to be h^2-*uniform* or *smooth*. That is; we assume there exists a constant σ independent of h, such that

$$|\boldsymbol{F}_E(\hat{x}, \hat{y})| = |\boldsymbol{x}_{00} + \boldsymbol{x}_{11} - (\boldsymbol{x}_{01} + \boldsymbol{x}_{10})| \leq \sigma h^2. \tag{6}$$

This condition is met if the grid refinement asymptotically leads to parallelogram cells. In particular, this is the case if an initial mesh is refined j times by dividing the sides of the previous mesh at the face midpoints. To see this, consider the quadrilateral cell in Figure 1. The cell is divided into four subelements by dividing each edge into two equal halves. Let all cells of $\mathcal{T}_h$ be refined in a similar manner. Thus, since the map (3) is linear along edges, this yields a uniform refinement. As h decreases, any element $E \in \mathcal{T}_h$ approaches a parallelogram. Let $\boldsymbol{x}_{ij}, i, j = 1, 2$, specify a given cell, and let a subcell be defined by $\boldsymbol{x}'_{ij}, i = 1, 2$. Then for the subsequent refinement level

$$|\boldsymbol{F}_E(\hat{x}, \hat{y})| = |\boldsymbol{x}'_{00} + \boldsymbol{x}'_{11} - (\boldsymbol{x}'_{01} + \boldsymbol{x}'_{10})| = \frac{1}{4}|\boldsymbol{x}_{00} + \boldsymbol{x}_{11} - (\boldsymbol{x}_{01} + \boldsymbol{x}_{10})|. \tag{7}$$

Hence, when the element size has been halved j times, $|\boldsymbol{F}_{\hat{x}\hat{y}}|$ is reduced by a factor of $(1/2)^{2j}$, and the mesh size $h = \frac{H}{2^j}$, where H is the mesh size of the original mesh. A further discussion of h^2-uniform grids can be found in [11].

3. $\mathcal{CVI}$ Finite Element Space

Let $V_h \times Q_h \subset H(\mathrm{div}, \Omega) \times L^2(\Omega)$. The following problem is then a discrete formulation of (2): *Find a pair* $(\boldsymbol{q}_h, p_h) \in V_h \times Q_h$ *such that*

$$\begin{aligned} (\boldsymbol{K}^{-1}\boldsymbol{q}_h, \boldsymbol{v}) - (p_h, \mathrm{div}\, \boldsymbol{v}) &= - < \boldsymbol{v} \cdot \boldsymbol{n}, p_0 >, \quad && \forall \boldsymbol{v} \in V_h, \\ (\mathrm{div}\, \boldsymbol{q}_h, u) &= (g, u), && \forall u \in Q_h. \end{aligned} \tag{8}$$

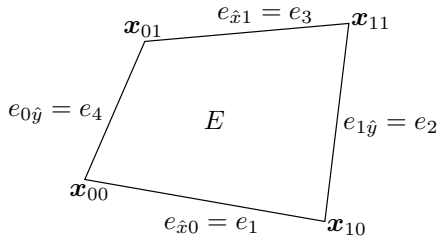

FIGURE 2. The corners and faces of a quadrilateral cell expressed in terms of the reference space coordinates $0 \leq \hat{x}, \hat{y} \leq 1$.

Let $\hat{\boldsymbol{v}}$ be a vector field in $H(\mathrm{div}, \hat{E})$. Then, the Piola transformation $\mathcal{P} = \mathcal{P}_E$ yields the natural way to represent a vector field $\boldsymbol{v} = \mathcal{P}_E \hat{\boldsymbol{v}} \in H(\mathrm{div}, E)$ by

$$\boldsymbol{v}(\boldsymbol{x}) = \mathcal{P}(\hat{\boldsymbol{x}})\hat{\boldsymbol{v}}(\hat{\boldsymbol{x}}) = \frac{1}{J}\boldsymbol{D}\hat{\boldsymbol{v}} \circ \boldsymbol{F}^{-1}(\boldsymbol{x}). \tag{9}$$

The Piola transformation relates the two vector fields so that the normal fluxes are preserved. If $p = \hat{p} \circ \boldsymbol{F}^{-1}$ for some $\hat{p} : \hat{E} \to \mathbb{R}$, we have

$$\int_e \boldsymbol{v} \cdot \boldsymbol{n}\, p\, ds = \int_{\hat{e}} \hat{\boldsymbol{v}} \cdot \hat{\boldsymbol{n}}\, \hat{p}\, d\hat{s}, \tag{10}$$

where $\boldsymbol{n}$ and $\hat{\boldsymbol{n}}$ are the outward unit normal vectors on ∂E and $\partial \hat{E}$, respectively. The construction of finite element subspaces of $H(\mathrm{div}, \Omega)$ necessitates continuity of normal fluxes. Let $\hat{V}_h \subset H(\mathrm{div}, \hat{E})$ denote the space of shape functions on a reference element $\hat{E}$. Thus, by applying (9) to some function $\hat{\boldsymbol{\psi}} \in V_h$, we obtain a shape function $\boldsymbol{\psi} \in V_h$ on E.

Henceforth, we let $P_{i,j}$ denote a piecewise polynomial of degree at most (i, j) in $(\hat{x}, \hat{y})$, respectively, associated with $\mathcal{T}_h$. The classical family of finite elements for $H(\mathrm{div})$ approximation is the Raviart-Thomas elements $\mathcal{RT}_r := P_{r+1,r}(\hat{E}) \times P_{r,r+1}(\hat{E}), r \geq 0$.

Here we consider the lowest-order Raviart-Thomas space $\mathcal{RT}_0$. Let $P_{0,0}$ denote piecewise constants on $(0,1) \times (0,1)$. On the reference square $\hat{E}$ the $\mathcal{RT}_0$ velocity space is defined as the four-dimensional space given as all vector fields of the following form

$$\mathcal{RT}_0(\hat{E}) = (P_{0,0} + \hat{x}P_{0,0}) \times (P_{0,0} + \hat{y}P_{0,0}).$$

Element wise, this gives rise to the following shape functions as functions of the reference space coordinates.

$$\boldsymbol{\psi}_i(\hat{\boldsymbol{x}}) = \mathcal{P}(\hat{x}, \hat{y})\hat{\boldsymbol{\psi}}_i(\hat{\boldsymbol{x}}), \tag{11}$$

for $i = 1, \ldots, 4$. Here $\hat{\boldsymbol{\psi}}_1 = [0, 1 - \hat{y}]^T$, $\hat{\boldsymbol{\psi}}_2 = [\hat{x}, 0]^T$, $\hat{\boldsymbol{\psi}}_3 = [0, \hat{y}]^T$ and $\hat{\boldsymbol{\psi}}_4 = [1 - \hat{x}, 0]^T$.

Finally, the space of scalar variables Q_h is simply given as

$$Q_h := \{u \in L_2 : \ u|_E \in P_0(E), \quad \forall\, E \in \mathcal{T}_h\}. \tag{12}$$

3.1. $\mathcal{CVI}$ Shape Functions. We will now define the $\mathcal{CVI}$ elements. Note, that for simplicity of exposition, we let $\mathcal{P}(\hat{x}, \hat{y}) = \mathcal{P}_{\hat{x}\hat{y}}$, with $\hat{x}, \hat{y} = 0$ or 1, from this point on, while $\phi_{ij} = \phi_{ij}(\hat{x}, \hat{y})$, $i, j = 0, 1$, is defined in Equation (4). Further, the numbering of the corners and faces are shown in Figure 2.

Definition 1.

$$\boldsymbol{\psi}_1^{cvi} = \mathcal{P}_{00}\begin{pmatrix}0\\ \phi_{00}\end{pmatrix} + \mathcal{P}_{10}\begin{pmatrix}0\\ \phi_{10}\end{pmatrix}, \tag{13}$$

$$\boldsymbol{\psi}_2^{cvi} = \mathcal{P}_{10}\begin{pmatrix}\phi_{10}\\ 0\end{pmatrix} + \mathcal{P}_{11}\begin{pmatrix}\phi_{11}\\ 0\end{pmatrix}, \tag{14}$$

$$\boldsymbol{\psi}_3^{cvi} = \mathcal{P}_{11}\begin{pmatrix}0\\ \phi_{11}\end{pmatrix} + \mathcal{P}_{01}\begin{pmatrix}0\\ \phi_{01}\end{pmatrix}, \tag{15}$$

$$\boldsymbol{\psi}_4^{cvi} = \mathcal{P}_{00}\begin{pmatrix}\phi_{00}\\ 0\end{pmatrix} + \mathcal{P}_{01}\begin{pmatrix}\phi_{01}\\ 0\end{pmatrix}. \tag{16}$$

The shape functions $\boldsymbol{\psi}_i^{cvi}$ are constructed to fulfill the next lemma.

Lemma 1. *Let $\boldsymbol{n}_j$, $j = 1, \ldots, 4$, be the (positive) normal vector to edge e_j of an element, with length equal to the length of e_j. Then*

$$\boldsymbol{\psi}_i^{cvi}(e_j) \cdot \boldsymbol{n}_j = \delta_{ij}.$$

Proof. We prove Lemma 1 for $\boldsymbol{\psi}_4^{cvi}$. The other $\boldsymbol{\psi}_i^{cvi}$, for $i = 1, \ldots, 3$, follow in a similar manner. From (9), we have $\mathcal{P}_{00} = \frac{1}{J_{00}}\boldsymbol{D}_{00}$, with $\boldsymbol{D}_{00}(\phi_{00}, 0)^T = (\boldsymbol{x}_{10} - \boldsymbol{x}_{00})\phi_{00}$. Now, $(\boldsymbol{x}_{10}-\boldsymbol{x}_{00})\cdot\boldsymbol{n}_1 = 0$, and $(\boldsymbol{x}_{10}-\boldsymbol{x}_{00})\cdot\boldsymbol{n}_4 = (\boldsymbol{x}_{10}-\boldsymbol{x}_{00})\times(\boldsymbol{x}_{01}-\boldsymbol{x}_{00}) = J_{00}$, while ϕ_{00} is zero along e_2 and e_3. Similarly, for $\mathcal{P}_{01}$ we have, $(\boldsymbol{x}_{11}-\boldsymbol{x}_{01})\cdot\boldsymbol{n}_3 = 0$, and $(\boldsymbol{x}_{11} - \boldsymbol{x}_{01}) \cdot \boldsymbol{n}_4 = J_{01}$, while ϕ_{01} is zero along e_1 and e_2. Hence, $\boldsymbol{\psi}_4^{cvi} \cdot \boldsymbol{n}_4 = (\phi_{00} + \phi_{01})$, which equals 1 along e_4, while $\boldsymbol{\psi}_4^{cvi}(e_j) \cdot \boldsymbol{n}_j = 0$ for $j = 2, 3, 4$. □

To more clearly see the relation to the $\mathcal{RT}_0$ elements, we provide the following lemma.

Lemma 2. *Let $\hat{\boldsymbol{\psi}}_i$, $i = 1, \ldots, 4$, be the $\mathcal{RT}_0$ shape functions on the element $\hat{E}$, see Equation (11). Then, we have*

$$\begin{aligned}
\boldsymbol{\psi}_1^{cvi}(\hat{x}, \hat{y}) &= \mathcal{P}_{00}\hat{\boldsymbol{\psi}}_1 + (\mathcal{P}_{10} - \mathcal{P}_{00})[0, \hat{x}(1-\hat{y})]^T,\\
\boldsymbol{\psi}_2^{cvi}(\hat{x}, \hat{y}) &= \mathcal{P}_{10}\hat{\boldsymbol{\psi}}_2 + (\mathcal{P}_{11} - \mathcal{P}_{10})[\hat{x}\hat{y}, 0]^T,\\
\boldsymbol{\psi}_3^{cvi}(\hat{x}, \hat{y}) &= \mathcal{P}_{01}\hat{\boldsymbol{\psi}}_3 + (\mathcal{P}_{11} - \mathcal{P}_{01})[0, \hat{x}\hat{y}]^T,\\
\boldsymbol{\psi}_4^{cvi}(\hat{x}, \hat{y}) &= \mathcal{P}_{00}\hat{\boldsymbol{\psi}}_4 + (\mathcal{P}_{01} - \mathcal{P}_{00})[(1-\hat{x})\hat{y}, 0]^T,
\end{aligned}$$

and for parallelogram cells, the $\mathcal{CVI}$ element degenerates to the $\mathcal{RT}_0$-element.

Proof. The proof of Lemma 2 follows immediately from Definition 1, and the fact that on parallelogram cells, the Piola mapping is constant. □

Finally, the $\mathcal{CVI}$ basis elements also fulfill exact representation of uniform flow, or equivalently, they preserve constant vector fields.

Lemma 3. *Let $\boldsymbol{e}_k$, $k = 1, 2$, be the unit vector, and $\boldsymbol{n}_i$ the (positive) edge normal with length equal to the edge length. Then the $\mathcal{CVI}$ basis functions for $i = 1, \ldots, 4$, fulfil*

$$\boldsymbol{e}_k = \sum_{i=1}^{4} f_{ki}\, \boldsymbol{\psi}_i^{cvi}, \tag{17}$$

with flux $f_{ki} = (\boldsymbol{e}_k \cdot \boldsymbol{n}_i)$.

Proof. For simplicity of notation, let $\boldsymbol{\xi}_i$ be the edge vector along edge e_i, such that $\boldsymbol{\xi}_1 = (\boldsymbol{x}_{10} - \boldsymbol{x}_{00})$, and let the vertices be indexed from 1 to 4 in counter-clockwise

direction, so that $i = 1$ corresponds to vertex x_{00}. Finally, let $i = 0$ or 5 correspond to $i = 4$ or 1. With this notation,

$$f_{k1}\,\boldsymbol{\psi}_1^{cvi} = (\boldsymbol{e}_k \cdot \boldsymbol{n}_1)\,\mathcal{P}_1 \begin{pmatrix} 0 \\ \phi_1 \end{pmatrix} + (\boldsymbol{e}_k \cdot \boldsymbol{n}_1)\,\mathcal{P}_2 \begin{pmatrix} 0 \\ \phi_2 \end{pmatrix},$$

where $\mathcal{P}_1 = \frac{1}{J(\boldsymbol{x}_1)}[\boldsymbol{\xi}_1, \boldsymbol{\xi}_4]$, and $\mathcal{P}_2 = \frac{1}{J(\boldsymbol{x}_2)}[\boldsymbol{\xi}_1, \boldsymbol{\xi}_2]$. Now,

$$\begin{aligned}
\sum_{i=1}^{4} f_{ki}\,\boldsymbol{\psi}_i^{cvi} &= \sum_{i=1}^{4} \frac{(\boldsymbol{e}_k \cdot \boldsymbol{n}_i)\,\boldsymbol{\xi}_{i-1}}{J(\boldsymbol{x}_i)}\phi_i + \sum_{i=1}^{4} \frac{(\boldsymbol{e}_k \cdot \boldsymbol{n}_i)\,\boldsymbol{\xi}_{i+1}}{J(\boldsymbol{x}_{i+1})}\phi_{i+1} \\
&= \sum_{i=1}^{4} \frac{(\boldsymbol{e}_k \cdot \boldsymbol{n}_{i+1})\,\boldsymbol{\xi}_i}{J(\boldsymbol{x}_{i+1})}\phi_{i+1} + \sum_{i=1}^{4} \frac{(\boldsymbol{e}_k \cdot \boldsymbol{n}_i)\,\boldsymbol{\xi}_{i+1}}{J(\boldsymbol{x}_{i+1})}\phi_{i+1} \\
&= \sum_{i=1}^{4} \left[\,(\boldsymbol{e}_k \cdot \boldsymbol{n}_{i+1})\,\boldsymbol{\xi}_i + (\boldsymbol{e}_k \cdot \boldsymbol{n}_i)\,\boldsymbol{\xi}_{i+1}\,\right] \frac{\phi_{i+1}}{J(\boldsymbol{x}_{i+1})}.
\end{aligned}$$

Since $\boldsymbol{e}_k$ is the unit vector;

$$(\boldsymbol{e}_k \cdot \boldsymbol{n}_{i+1})\,\boldsymbol{\xi}_i + (\boldsymbol{e}_k \cdot \boldsymbol{n}_i)\,\boldsymbol{\xi}_{i+1} = \frac{1}{2}\left(\boldsymbol{\xi}_i \boldsymbol{n}_{i+1}^T + \boldsymbol{\xi}_{i+1}\boldsymbol{n}_i^T\right)\boldsymbol{e}_k.$$

Note that all vectors are taken in positive direction with regards to the reference space. Thus, with $\boldsymbol{\xi}_i = [\xi_i^1, \xi_i^2]^T = \pm[n_i^2, -n_i^1]^T$, we have

$$\left(\boldsymbol{\xi}_i \boldsymbol{n}_{i+1}^T + \boldsymbol{\xi}_{i+1}\boldsymbol{n}_i^T\right)/2 = J(\boldsymbol{x}_{i+1})\boldsymbol{I},$$

with $\boldsymbol{I}$ the identity matrix. Summing up and using eq. (5),

$$\sum_{i=1}^{4} f_{ki}\,\boldsymbol{\psi}_i^{cvi} = \sum_{i=1}^{4} J(\boldsymbol{x}_{i+1})\boldsymbol{I}\,\boldsymbol{e}_k\,\frac{\phi_{i+1}}{J(\boldsymbol{x}_{i+1})} = \boldsymbol{e}_k \sum_{i=1}^{4} \phi_i = \boldsymbol{e}_k.$$

□

For each cell, the $\mathcal{CVI}$ basis functions can also be viewed as barycentric edge based $H(\mathrm{div})$ coordinates. In this sense, Equation (17) is analogous to Equation (5).

3.2. Hexahedral 3D Mesh. We limit the 3D discussion to shape-regular hexahedral cells, with six faces and eight vertices. Extension of face based elements from 2D to 3D is unfortunately a bit more complicated from quadrilaterals to hexahedra, than from triangulations to tetrahedra. In 2D, both quadrilaterals and triangulations have two vertices per edge, while in 3D, a hexahedral face has four vertices compared to three on a tetrahedral face. This implies that the adjacent edge vectors to a vertex do not provide us enough information for a definition of the face for a hexahedral element. As we will show below, we need to provide additional information.

Due to the result of [19], which proves that for a general hexahedron with bilinear faces, both a local reconstruction of velocity based on the six faces and reproduction of uniform flow cannot be satisfied in $H(\mathrm{div}, \Omega)$, the $\mathcal{CVI}$ shape functions are limited to grids with planar faces henceforth. We note that even when this is the case, the $\mathcal{RT}_0$ elements are generally not able to preserve uniform flow. An example is a grid of truncated pyramids [16].

Let $\hat{\boldsymbol{x}} = (\hat{x}, \hat{y}, \hat{z}) \in \mathbb{R}^3$ denote a point in the reference space. A hexahedron in physical space is represented as the image of a reference element $\hat{E}$ under the trilinear map $\boldsymbol{H} = \boldsymbol{H}_E : \hat{E} \to E$. Here, $\hat{E} = \{\hat{\boldsymbol{x}}\,|0 \le \hat{x}, \hat{y}, \hat{z} \le 1\}$ is the unit cube. Let $\boldsymbol{x}_{ijk}, i, j, k = 0, 1$, be the vertices of the physical hexahedron E, where the index

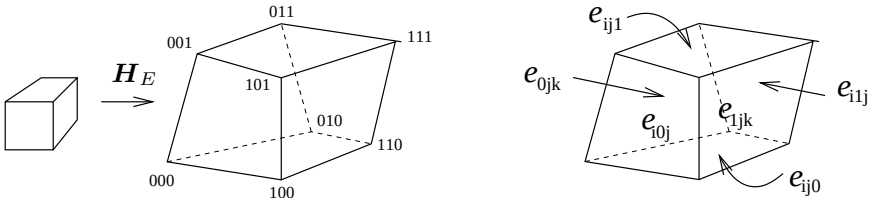

(a) The map $\boldsymbol{H}_E$ and the vertex numbering.

(b) Illustration of the face numbering.

FIGURE 3. A physical element E is the image under the trilinear map $\boldsymbol{H}_E$ from a reference element $\hat{E}$.

refers to the corresponding $(\hat{x}, \hat{y}, \hat{z})$ value. Then, under the map $\boldsymbol{H}_E$, any point $\boldsymbol{x} \in E$ is given as

$$\boldsymbol{x}(\hat{x}, \hat{y}, \hat{z}) = \sum_{ijk=1}^{2} \boldsymbol{x}_{ijk} \phi_{ijk}(\hat{x}, \hat{y}, \hat{z}), \tag{18}$$

where $\phi_{ijk}(\hat{x}, \hat{y}, \hat{z})$ is the trilinear node functions on $\hat{E}$, or barycentric basis functions. That is; $\phi_{ijk}(\boldsymbol{x}_{lmn}) = \delta_{(ijk)(lmn)}$ and $\sum \phi_{ijk} = 1$ on E.

We number the columns of the Jacobian matrix of $\boldsymbol{H}_E$ from 1 to 3, i.e. $\boldsymbol{D} = [\boldsymbol{D}^1, \boldsymbol{D}^2, \boldsymbol{D}^3]$, and we evaluate the Jacobian matrix at the eight vertices $\boldsymbol{x}_{ijk}$, $i, j, k = 0, 1$. Further, we denote the faces by the four vertex indices defining the face, e.g., the face with the four vertices $\boldsymbol{x}_{0jk}$, $j, k = 0, 1$, will be indexed by $0jk$. We denote the face area A_{ijk} and the unit normal $\bar{\boldsymbol{n}}_{ijk}$ in the same manner. Note that the unit normals are always orientated in the positive reference space direction.

For a definition of face elements in accordance with an analogue of Lemma 1, note that the Jacobian determinant of the trilinear mapping $\boldsymbol{H}_E$ evaluated at a vertex $\boldsymbol{x}_{ijk}$, does not provide us with enough information. Therefore, we define the diagonal matrix

$$\begin{aligned} \bar{J}_{ijk} = \operatorname{diag}(&\boldsymbol{D}^1_{ijk} \cdot \bar{\boldsymbol{n}}_{\hat{i}jk} A_{\hat{i}jk}, \\ &\boldsymbol{D}^2_{ijk} \cdot \bar{\boldsymbol{n}}_{i\hat{j}k} A_{i\hat{j}k}, \\ &\boldsymbol{D}^3_{ijk} \cdot \bar{\boldsymbol{n}}_{ij\hat{k}} A_{ij\hat{k}}), \end{aligned} \tag{19}$$

for $i, j, k = 0, 1$. Here, hats indicate indices pointing to faces. Similarly, we define

$$\bar{\mathcal{P}}_{ijk} = \boldsymbol{D}_{ijk} \bar{J}^{-1}_{ijk}.$$

Due to the limitation to planar faces, observe that $\boldsymbol{v} \cdot \bar{\boldsymbol{n}}_{ijk} A_{ijk}$ on a face e_{ijk} corresponds to the face flux. Now, on the six faces of a hexahedron, the $\mathcal{CVI}$ shape functions can be defined by

Definition 2.

$$\boldsymbol{\psi}^{cvi}_{\alpha jk} = \sum_{jk=0}^{1} \bar{\mathcal{P}}_{\alpha jk} \begin{pmatrix} \phi_{\alpha jk} \\ 0 \\ 0 \end{pmatrix}, \quad \textit{for face } e_{\alpha jk},\ \alpha = 0, 1, \tag{20}$$

$$\boldsymbol{\psi}^{cvi}_{i\alpha k} = \sum_{ik=0}^{1} \bar{\mathcal{P}}_{i\alpha k} \begin{pmatrix} 0 \\ \phi_{i\alpha k} \\ 0 \end{pmatrix}, \quad \textit{for face } e_{i\alpha k},\ \alpha = 0, 1, \tag{21}$$

$$\boldsymbol{\psi}^{cvi}_{ij\alpha} = \sum_{ij=0}^{1} \bar{\mathcal{P}}_{ij\alpha} \begin{pmatrix} 0 \\ 0 \\ \phi_{ij\alpha} \end{pmatrix}, \quad \textit{for face } e_{ij\alpha},\ \alpha = 0, 1. \tag{22}$$

With Definition 2, we can immediately provide a lemma analogous to Lemma 1.

Lemma 4. *Let the six faces of a hexahedron be denoted by e_{lmn}, with $l, m, n = 0, 1$. Then*

$$\boldsymbol{\psi}^{cvi}_{ijk}(e_{lmn}) \cdot \boldsymbol{n}_{lmn} A_{lmn} = \delta_{(ijk)(lmn)}.$$

Proof. It holds to prove Lemma 4 for one face. For $\boldsymbol{\psi}^{cvi}_{0jk}$, we start with the vertex at $\boldsymbol{x}_{000}$, where $\boldsymbol{D}_{000}(\phi_{000}, 0, 0)^T = (\boldsymbol{x}_{100} - \boldsymbol{x}_{000})\phi_{000}$. Further, from the Definition (19) $(\boldsymbol{x}_{100} - \boldsymbol{x}_{000}) \cdot \boldsymbol{n}_{0jk} A_{0jk} = (\bar{J}_{000})_{1,1}$, and $(\boldsymbol{x}_{100} - \boldsymbol{x}_{000}) \cdot \boldsymbol{n}_{i0k} = (\boldsymbol{x}_{100} - \boldsymbol{x}_{000}) \cdot \boldsymbol{n}_{ij0} = 0$, while ϕ_{000} is zero on face e_{1jk}, e_{i1k} and e_{ij1}. A similar derivation applies to the other three vertices of e_{0jk}. It follows that $\boldsymbol{\psi}^{cvi}_{0jk} \cdot \boldsymbol{n}_{0jk} A_{0jk} = \sum_{jk=0}^{1} \phi_{0jk}$, which is 1 on face e_{0jk}, while $\boldsymbol{\psi}^{cvi}_{0jk} \cdot \boldsymbol{n}_{lmn} = 0$ for the other five faces. □

In [18], a first version of one of the $\mathcal{CVI}$ shape functions for hexahedral cells was defined. There, a counterexample on coercivity of $(\boldsymbol{K}^{-1}\boldsymbol{v}, \boldsymbol{v})$ in the full $H(\mathrm{div})$ norm was presented.

A lemma analogous to Lemma 3 can be stated also for the $\mathcal{CVI}$ space in 3D. Due to the properties of the barycentric coordinates, we have that the $\mathcal{CVI}$ elements preserve uniform flow. The details are omitted here.

3.3. Deficiencies. The $\mathcal{CVI}$ finite elements do represent uniform flow exactly, but the price to pay is that the divergence of the $\mathcal{CVI}$ elements is not contained in the discrete pressure space of cellwise constants. This means that

$$\mathrm{div}(\boldsymbol{v}^{cvi}) \not\subset Q_h.$$

Define the interpolation, $P_h : L^2 \to Q_h$, and as L^2-interpolation, $\Pi^{cvi} : H(\mathrm{div}) \to \mathcal{CVI}$, by $(\mathrm{div}(\Pi^{cvi}\boldsymbol{v} - \boldsymbol{v}), u)$ for all $u \in Q_h$. Then, we do not meet the commutative hypothesis, i.e.; $P_h \,\mathrm{div}\, \boldsymbol{v} \neq \mathrm{div}\, \Pi^{cvi}\boldsymbol{v}$ for $\boldsymbol{v} \in H(\mathrm{div})$. For classical mixed finite elements, like the Raviart-Thomas elements or the Brezzi-Douglas-Marini elements, this is usually fulfilled. These properties play an essential part in the analysis of the classical mixed methods, however, this hypothesis may be too strong a requirement.

4. Numerical Examples

In this section, we illustrate the convergence of the $\mathcal{CVI}$ mixed finite element space by simulations on smooth grids. A definition of smooth meshes was given in section 2. We employ a sequence of the mesh shown in Figure 4.

The errors are measured in discrete L^2 norms for both variables. Let A_E be the area of a grid cell $E \in \mathcal{T}_h$. Then, for the pressure, we define

$$\|p - p_h\|_{(L^2,h)} = \left(\frac{\sum_{E \in \mathcal{T}_h} A_E (p_E - p_{h,E})^2}{\sum_{E \in \mathcal{T}_h} A_E} \right)^{1/2}.$$

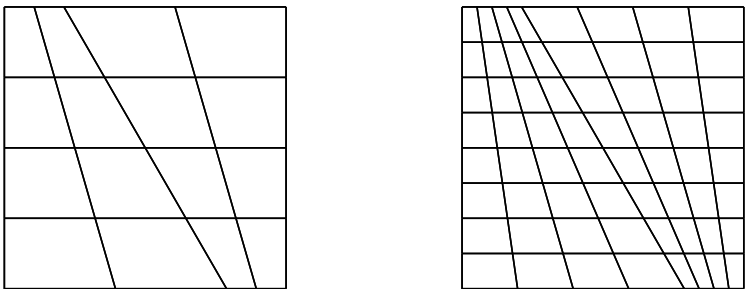

FIGURE 4. Smooth refinement of grid.

Let W_e be the area associated to an edge $e \in \mathcal{E}_h$. Here, W_e is set to be half the area sum of the two cells adjacent to edge e. Then, the discrete L^2 norm for the normal velocities are given by

$$\|q - q_h\|_{(L^2,h)} = \left(\frac{\sum_{e\in\mathcal{E}_h} W_e((q_e - q_{h,e})/|e_h|)^2}{2\sum_{e\in\mathcal{E}_h} W_e} \right)^{1/2},$$

where q_e is the normal velocity across the edge e. We also provide the results measured in discrete maximum norm.

We note that since, by construction, the $\mathcal{CVI}$ method preserves a constant flow field, it is expected to return the exact solution for a linear pressure field. Moreover, for parallelogram grids, the $\mathcal{CVI}$ scheme degenerates exactly to the $\mathcal{RT}_0$ interpolation. Thus, numerical results should be identical for the two discretizations for such grids. This is observed in the simulations.

First, we apply the smooth solution

$$u(x, y) = \cosh(\pi x)\, \cos(\pi y), \tag{23}$$

where we assume the permeability to be the identity matrix. The discrete L^2 convergence is seen in Figure 5(a). We observe that both the pressure and the normal velocity converge as h^2 in discrete L^2 norm. The results in maximum norm is seen in Figure 5(b)

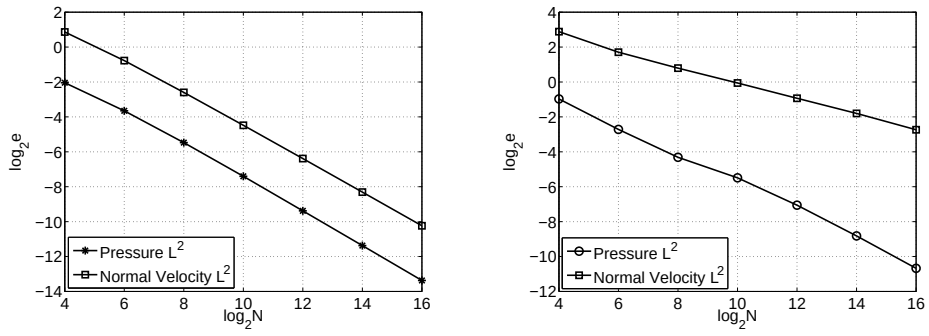

(a) Results in discrete L^2 norm.

(b) Results in discrete L^∞ norm.

FIGURE 5. Numerical convergence of solution (23). N is the number of elements in each direction.

The next cases apply to a more realistic simulation where we let the permeability vary throughout the domain. Denote the four regions in our domain from 1 to 4, as

seen in Figure 6. We may impose different conductivities in the four regions, which again may render a singularity at the corner where they meet.

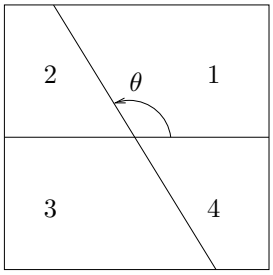

FIGURE 6. Regions 1 to 4 may have different permeabilities.

First, we assume an isotropic, heterogeneous medium, and let the conductivities in region 2, 3 and 4 equal. If r is the distance from the corner, and θ denotes the angle from the x-axis, we have the following analytical solution

$$u(r,\theta) = r^{\alpha} \begin{cases} \cos\alpha(\theta - \pi/3) & \text{for } \theta \in [0,\, 2\pi/3], \\ d\cos\alpha(4\pi/3 - \theta) & \text{for } \theta \in [2\pi/3,\, 2\pi], \end{cases} \tag{24}$$

where $\alpha = (3/\pi)\arctan\sqrt{1+2/\kappa}$ and $d = \cos(\alpha\pi/3)/\cos(2\alpha\pi/3)$. Denote by $\kappa = k_1/k_2$ the conductivity ratio. Here, k_1 is the permeability for region 1 and k_2 for the rest of the medium. We have $\kappa \geq 0$, which yields $\alpha \in [0.75,\, 1.5]$. This parameter describes the regularity of the solution, that is; we find that the solution (24) belongs to the space $H_{\pi}^{1+\alpha-\epsilon}$ for an arbitrary $\epsilon > 0$. Here, the subscript π means that we operate in interpolated Hilbert spaces [25].

Let $\kappa = 10^{-3}$ and 10^2, and thus we have $\alpha \approx 1.4787$ and $\alpha \approx 0.7547$, respectively. The convergence behavior in discrete L^2 norm and discrete maximum norm can be found in Figures 7(a) and 7(b), respectively.

Further, we let the conductivities in regions 1 and 3 equal, and similarly, regions 2 and 4 have the same conductivities. We still assume an isotropic permeability. This accommodates a solution where $\alpha \in [0, 1.5]$, and moreover it satisfies $u(r,\theta) =$

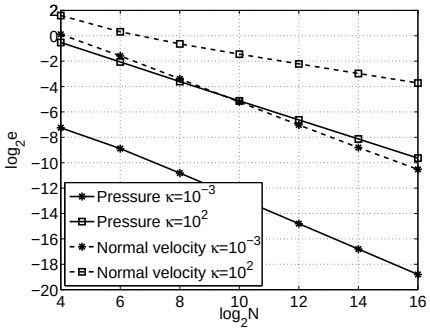

(a) Estimates in discrete L^2 norm.

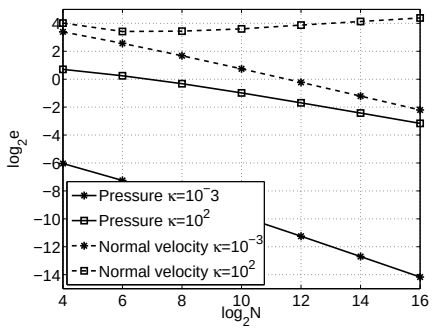

(b) Estimates in discrete L^{∞} norm.

FIGURE 7. Numerical convergence for solution (24) with $\kappa = 10^{-3}$ and 10^2, respectively. N is the number of grid cells.

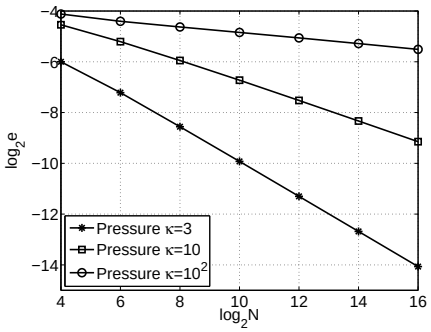

(a) Estimates in discrete L^2 norm for the pressure variable.

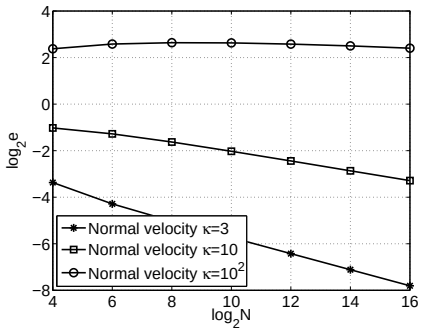

(b) Estimates in discrete L^2 norm for the normal velocity.

FIGURE 8. Numerical L^2 convergence for solution (25) with $\kappa = 3, 10$ and 10^2, respectively. N is the number of grid cells.

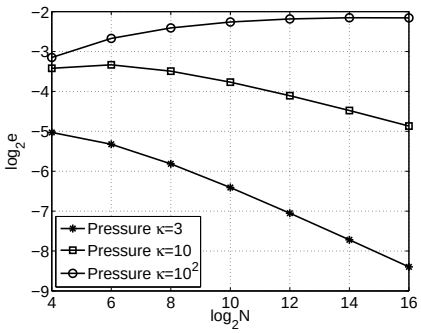

(a) Estimates in discrete L^∞ norm for the pressure variable.

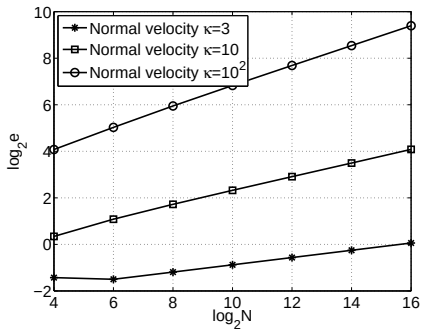

(b) Estimates in discrete L^∞ norm for the normal velocity.

FIGURE 9. Numerical L^∞ convergence for solution (25) with $\kappa = 3, 10$ and 10^2, respectively. N is the number of grid cells.

$-u(r, \theta - \pi)$. The solution reads

$$u(r,\theta) = r^\alpha \begin{cases} \cos\alpha\,(\theta - \pi/3) & \text{for } \theta \in [0,\, 2\pi/3], \\ d\sin\alpha\,(5\pi/6 - \theta) & \text{for } \theta \in [2\pi/3,\, \pi], \end{cases} \tag{25}$$

and here $\alpha = (6/\pi)\arctan(1/\sqrt{1+2\kappa})$ and $d = \cos(\alpha\pi/3)/\sin(\alpha\pi/6)$. We choose conductivity ratios of 3, 10 and 100 to illustrate the convergence behavior for various regularities of the solution (25). This is seen in Figures 8 and 9 for estimates in discrete L^2 and L^∞ norm, respectively.

We can summarize the observed convergence rates for solution (23), (24) and (25), the latter two for various values of the parameter α, as follows. Measured in discrete L^2 norm we find, for the potential, the relation

$$\|p - p_h\|_{(L^2,h)} \sim h^{\min\{2,2\alpha\}}. \tag{26}$$

For the normal velocity we have

$$\begin{aligned} \|q - q_h\|_{(L^2,h)} &\sim h^2, \qquad \text{for } p \in H^2, \\ \|q - q_h\|_{(L^2,h)} &\sim h^\alpha, \qquad \text{else.} \end{aligned} \tag{27}$$

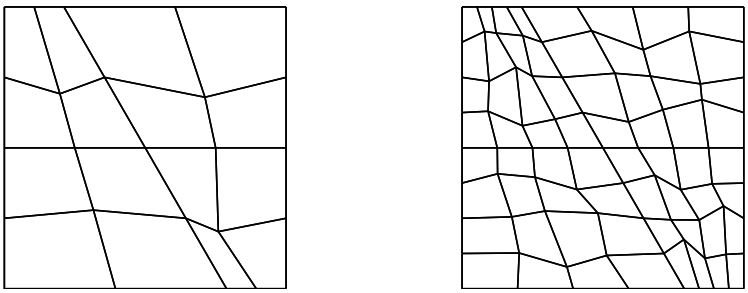

FIGURE 10. Rough grid. Each cell is distorted by $\mathcal{O}(h)$ at each refinement level.

This is in consistency with the finite element theory [25]. Similar results for some control-volume multipoint flux approximation methods can be found in [1].

For geophysical applications, rough grids honoring the geology are often required for accurate simulations. Thus, it is appropriate to apply such meshes to the $\mathcal{CVI}$ method presented here. By a rough grid, or h-perturbed grid, we mean a sequence of grids not approaching parallelograms as the grid is refined, see Figure 10. At every refinement level, each element is randomly distorted by $\mathcal{O}(h)$, with h being the maximum element edge. The $\mathcal{CVI}$ method is seen not to yield a convergent approximation to any of the solutions for h-perturbed meshes, whereas the $\mathcal{RT}_0$ elements converges in discrete L^2 norm also for the rough meshes. Note that, according to analysis, if measured in full $H(\mathrm{div}, \Omega)$ norm, the $\mathcal{RT}_0$ velocity space will not convergence for rough meshes either.

Finally, we remark that the implementation of the $\mathcal{CVI}$ velocity space is much more comprehensive than the $\mathcal{RT}_0$ elements.

5. Discussion

In this work, we have presented an analysis of the $\mathcal{CVI}$ elements as velocity elements in a mixed finite element setting. The $\mathcal{CVI}$ shape functions are derived both in 2D and 3D. Numerical convergence behavior is provided for the $\mathcal{CVI}$ space on smooth quadrilateral grids.

In 2D, we have seen that the $\mathcal{CVI}$ elements fulfill Lemma 1 - 3. That is; the $\mathcal{CVI}$ velocity space lies in $H(\mathrm{div})$, and is closely related to the $\mathcal{RT}_0$ space. In fact, for parallelogram shaped meshes, the $\mathcal{CVI}$ space degenerates to the $\mathcal{RT}_0$ space. Finally, by Lemma 3, the method preserves uniform flow. For the $\mathcal{CVI}$ functions in 3D, we can show that the same property applies.

However, since the divergence of the $\mathcal{CVI}$ velocity space is not contained in the space of constant pressures, it does not meet the commutative qualities, which is an essential part in classical analysis of the $\mathcal{RT}_0$ mixed method. Thus, compared to the $\mathcal{RT}_0$ method, we would expect some drawbacks of the proposed $\mathcal{CVI}$ method. This is also observed in the numerical simulations, where the $\mathcal{CVI}$ elements exhibit convergence in discrete L^2 norm for h^2-uniform grids, contrary to h-perturbed grids, where the elements do not convergence.

Acknowledgment. The authors would like to thank M. Nome for helpful discussions.

References

[1] I. Aavatsmark, G. T. Eigestad, and R. A. Klausen. Numerical convergence of the MPFA for general quadrilateral grids in two and three dimensions. IMA Vol. Ser. 142; *Compatible Spatial Discretizations for Partial Differential Equations* 1–22, 2006.

[2] D. N. Arnold, D. Boffi, and R. S. Falk. Quadrilateral H(div) finite elements. *SIAM J. Numer. Anal.*, 42(6):2429–2451, 2004.

[3] A. Bermùdes, P. Gamallo, M. Nogueiras, and R. Rodríguez. Approximation properties of lowest-order hexahedral Raviart-Thomas finite elements. *CR Math.*, 340(9):687–692, 2005.

[4] F. Brezzi and M. Fortin. *Mixed and Hybrid Finite Element Methods*. Springer series in computational mathematics. Springer-Verlag, 1991.

[5] P. G. Ciarlet. *The Finite Element Method for Elliptic Problems*. Noth-Holland Publishing Company, 1997.

[6] C. Cordes and W. Kinzelbach. Continuous groundwater velocity fields and path lines in linear, bilinear, and trilinear finite elements. *Water Resour. Res.*, 28(11):2903–2911, 1992.

[7] A. Datta-Gupta, M. J. King. *Streamline Simulation: Theory and practice*. SPE Textbook Series Vol. 11, 2007.

[8] H. Hægland, H. K. Dahle, G. T. Eigestad, K.-A. Lie, and I. Aavatsmark. Improved streamlines and time-of-flight for streamline simulation on irregular grids. *Adv. Water Resour.*, 30:1027–1045, 2007.

[9] E. Jimenez, K. Sabir, A. Datta-Gupta, and M. J. King. Spatial error and convergence in streamline simulation. *SPE Res. Eval. & Engrg*, 10(3):221–232, 2007. SPE 92873.

[10] R. Juanes and S. F. Matringe. Unified formulation for high-order streamline tracing on two-dimensional unstructured grids. *J. Sci. Comput.*, 38(1):50–73, 2009.

[11] R. A. Klausen and R. Winther. Convergence of multipoint flux approximations on quadrilateral grids. *Numer. Methods Partial Diff. Eqns.*, 22(6):1438–1454, 2006.

[12] R. A. Klausen and R. Winther. Robust convergence of multipoint flux approximation on rough grids. *Numer. Math.*, 104(3):317–337, 2006.

[13] S. F. Matringe and M. G. Gerritsen. On accurate tracing of streamlines. In *Proc. SPE Annual Technical Conference and Exhibition*, Houston, Texas, September 2004.

[14] S. F. Matringe, R. Juanes, and H. A. Tchelepi. Robust streamline tracing for the simulation of porous media flow on general triangular and quadrilateral grids. *J. Comput. Phys.*, 219(2):992–1012, 2006.

[15] S. F. Matringe, R. Juanes, and H. A. Tchelepi. Streamline tracing on general triangular and quadrilateral grids. *SPE J.*, 12(2):217–223, 2007. SPE 96411.

[16] R. L. Naff, T. F. Russell, and J. D. Wilson. Shape functions for velocity interpolation in general hexahedral cells. *Comput. Geosci.*, 6(3-4):285–314, 2002.

[17] J. C. Nédélec. Mixed finite elements in $\mathbb{R}^3$. *Numer. Math.*, 35:315–41, 1980.

[18] M. A. Nome. An analysis of the corner velocity interpolation as the approximation space in a mixed finite element method. Master's thesis, Department of Mathematics, University of Bergen, 2008.

[19] J. M. Nordbotten and H. Hægland. On reproducing uniform flow exactly on general hexahedral cells using one degree of freedom per surface. *Adv. Water Resour.*, 32(2): 264–67, 2009.

[20] M. Prévost. *Accurate coarse reservoir modeling using unstructured grids, flow-based upscaling and streamline simulation*. PhD thesis, Stanford University, 2003.

[21] M. Prévost, M. G. Edwards, and M. J. Blunt. Streamline tracing on curvilinear structured and unstructured grids. *SPE J.*, 7(2):139–148, 2002.

[22] P. A. Raviart and J. M. Thomas. A mixed finite element method for second order elliptic equations. In I. Galligani and E. Magenes, editors, *Mathematical Aspects of Finite Element Methods*, volume 606, pages 292–315. Springer-Verlag, 1977.

[23] A. Sboui, J. Jaffré, and J. E. Roberts. A composite mixed finite element for general hexahedral grids. Technical report, INRIA, September 2007.

[24] J. Shen. Mixed finite element method on distorted rectangular grids. Technical report, Texas A&M University, 1994.

[25] G. Strang and G. J. Fix. *An Analysis of the Finite Element Method*. Prentice-Hall, 1973.

[26] J. M. Thomas. *Sur l'analyse Numérique des Methodes d'eléments Finis Hybrides et Mixtes*. PhD thesis, Thése d'Etat, Université Pierre et Marie Curie, Paris, 1977.

[27] J. Wang and T. Mathew. Mixed finite element method over quadrilaterals. In I. Dimov, B. Sendov, and P. Vassilevski, editors, *Advances in numerical methods and applications: proceedings of the third international conference*. World Scientific, River edge, NJ, 1994.

Centre for Mathematics for Applications, University of Oslo, P.O. Box 1053 Blindern, N-0316 Oslo, Norway
E-mail: r.a.klausen@cma.uio.no

Department of Mathematics, Centre for Integrated Petroleum Research, University of Bergen, Bergen, Norway

Department of Mathematics, University of Bergen, P.O. Box 7803, N-5020 Bergen, Norway
E-mail: helge.dahle@math.uib.no